Fatigue and post-fatigue behavior of PBO FRCM-concrete joints

T. D'Antino [a], C. Carloni [b,*], L.H. Sneed [c], C. Pellegrino [d]

[a] University of Patras, Rio Achaia, Patras 26504, Greece
[b] University of Bologna, Viale Risorgimento 2, Bologna 40136, Italy
[c] Missouri S&T, 1401 North Pine Street, Rolla, MO 65409, USA
[d] University of Padova, via Marzolo 9, Padova 35131, Italy

Received 14 February 2015
Received in revised form 10 June 2015
Accepted 13 June 2015
Available online 20 June 2015

1. Introduction

Fiber-reinforced composite materials have been used extensively in recent decades to strengthen existing reinforced concrete (RC) structures. Fiber-reinforced polymer (FRP) composites, comprised of high-strength fibers impregnated by and applied by means of a thermosetting organic resin, are largely employed to strengthen and retrofit RC structures. Despite their numerous advantages, such as high strength-to-weight ratio, resistance to corrosion, and ease of installation, FRP composites present some disadvantages related to the use of organic matrices, such as change in the properties when the temperature is close to or above the matrix glass transition temperature, poor resistance to UV exposure, and no permeability compatibility with respect to the concrete support. Newly-developed fiber-reinforced cementitious matrix composites (FRCM) represent a promising alternative to FRP composites. They are comprised of high strength fibers embedded within a cementitious matrix that is responsible for the stress-transfer between the fibers and between the fibers and the support. The use of an inorganic matrix overcomes some of the issues related to the use of a thermosetting organic matrix. The type of matrix utilized in FRCM composites generally has:(1) high resistance to fire and high temperatures; (2) resistance to UV radiation; (3) ease of handling during the application because the inorganic binder is water-based; (4) permeability compatibility with the concrete substrate; and (5) unvarying workability time (between 4 °C and 40 °C). FRCM composites are still fairly new, and few experimental and analytical papers are available in the literature. FRCM composites have been proven to be effective for flexural strengthening [1–5], shear strengthening [6–8], and for confinement of RC members subjected to axial load or axial load and bending moment [9–12].

Although some authors have attempted to investigate the bond behavior of FRCM-concrete joints subjected to a quasi-static monotonic loading condition [13–18], a study of the fatigue behavior of FRCM composites is not available in the literature. Fatigue life assessment is of particular importance for strengthening and retrofitting applications of RC structures subject to cyclic or fatigue load, such as highway or railroad bridges. Studies conducted on RC elements strengthened by externally bonded FRP composites showed an increase of the fatigue life due to the redistribution of the stresses from the internal steel reinforcement to the FRP composite [19]. It is generally recognized that fatigue loading may cause interfacial crack growth, referred to as sub-critical crack growth, at load levels lower than the corresponding quasi-static load-carrying capacity [20]. To overcome this issue, Diab et al.

* Corresponding author. Tel.: +39 051 209 3492; fax: +39 051 209 3495.
E-mail addresses: dantino@upatras.gr (T. D'Antino), christian.carloni@unibo.it (C. Carloni), sneedlh@mst.edu (L.H. Sneed), carlo.pellegrino@unipd.it (C. Pellegrino).

[21] proposed to limit the maximum applied load in the case of FRP applications to 30% of the corresponding static load-carrying capacity. To prevent fatigue failure, ACI 440.2R-08 [22] recommends limiting the stress level in the FRP to $0.20f_{fu}$, $0.30f_{fu}$, and $0.55f_{fu}$ for glass, aramid, and carbon FRP, respectively, where f_{fu} is the design monotonic failure stress. The Japan Society of Civil Engineers (JSCE) [23] recommends reducing the interface fracture energy by a factor of 0.7 in the case of fatigue loading, which results in a reduction of the design applied stress level by a factor of 0.84 with respect to the monotonic load-carrying capacity [24].

For metals, it is well known that the fatigue limit, i.e. the number of cycles corresponding to failure N_f, is an increasing function of the loading frequency. Indeed, increased frequency has been observed to result in a lower crack growth rate, which therefore leads to a longer fatigue life [25]. Several authors have recognized the influence of the load frequency on concrete specimens subjected to compressive fatigue loading and proposed different analytical models to take this influence into account. In general, the analytical models available in the literature indicate that the fatigue life of concrete specimens increases with increasing frequency for a given applied stress range [26–28]. This behavior is explained in part by the presence of creep effects that become predominant particularly in the case of high stress level associated with low frequency [29]. Saucedo et al. [27] employed a Weibull Cumulative Distribution Function to relate the fatigue life of concrete cubic specimens subjected to cyclic compressive loading to the loading frequency, stress ratio, and number of cycles. Medeiros et al. [28] applied the same approach to study the effect of the loading frequency on plain and fiber-reinforced concrete cubes, observing that lowering loading frequency reduces the fatigue life especially in plain concrete. Although the behavior of plain and reinforced concrete beams subjected to fatigue loading has been studied by different authors [30–34], often the effect of the loading frequency was not considered. It should be noted that the effect of frequency was studied mostly in concrete specimens subjected to compression, and very limited studies regarding tensile fatigue are available in the literature.

This paper presents the results of an experimental campaign conducted on FRCM-concrete joints subjected to fatigue load with different frequencies and load ranges using a single-lap direct-shear test set-up. The FRCM composite is comprised of poly-paraphenylene benzobisoxazole (PBO) fibers embedded within a cementitious polymer modified matrix. Since it has been observed that civil engineering structures are usually loaded at frequencies between 1 and 5 Hz [35], the experimental tests were conducted using three different frequencies, namely 1 Hz, 3 Hz, and 5 Hz. Because studies conducted on RC beams strengthened with externally bonded FRP composites and subjected to cyclic load showed an influence of the load range on the fatigue response [30,31], this paper investigates the behavior of FRCM-concrete joints subjected to three different load ranges, namely 20–50%, 35–65%, and 20–65%. The percentages of the fatigue load range employed were computed with respect to the peak (ultimate) load obtained from quasi-static tests conducted on specimens with the same geometry and material characteristics and using the same test set-up [36]. The effect of the frequency on the fatigue behavior is investigated through a fracture mechanics approach.

2. Test set-up and materials employed

Fifteen single-lap direct-shear tests were conducted on PBO FRCM-concrete joints under cyclic loading using the classical push–pull configuration [37]. The test set-up employed was previ-ously used by the authors to conduct quasi-static monotonic direct-shear tests on FRCM-concrete joints that employed the same materials [15–17,36]. The single-lap configuration was employed for its simplicity and because it allows for direct measurement of the force in the composite. In addition, comparison between single- and double-lap shear tests carried out by the authors showed that the eccentricity of the applied load with respect to the support restraint in the single-lap configuration did not affect the results for specimens with a long bonded length [38]. The con-crete blocks used were 125 mm deep, 125 mm wide, and 375 mm long and were restrained by a steel frame bolted to the base of a servo-hydraulic universal testing machine (Fig. 1). The FRCM com-posite, comprised of one layer of a bidirectional PBO fiber net (the width b^* and thickness t^* of a single fiber bundle were equal to 5 mm and 0.092 mm, respectively) embedded within two 4 mm thick layers of cementitious matrix, was applied to one face of the concrete block. The bonded region started at a distance of 38 mm from the edge of the block at the loaded end. The face of the concrete block was sandblasted before the composite applica-tion to improve bond between the FRCM and the support. The bonded length and bonded width were 330 mm and 60 mm, respectively. The fibers were left bare outside the bonded area, and two through-bolted aluminum plates were bonded with epoxy resin to the end of the bare fiber net to improve gripping during testing. It should be noted that the fibers extended beyond the bonded area at the free end (Fig. 1a). The longitudinal fiber bun-dles, which are not woven with the transversal fibers, were ori-ented toward the internal layer of matrix that was directly applied to the concrete block.

All materials employed were tested in order to determine their mechanical properties. The same concrete blocks previously employed by the authors for the quasi-static tests [15,36] were sandblasted and used for the fatigue specimens. The concrete average compressive strength and average tensile strength were 42.5 MPa (CoV = 0.013) and 3.4 MPa (CoV = 0.113), respectively [17]. The fiber average tensile strength, average elastic modulus, and average ultimate strain, obtained by the authors, were 3010 MPa (CoV = 0.068), 206 GPa (CoV = 0.065), and 0.0145 (CoV = 0.104), respectively [16]. The specimens were cast at differ-ent times in small groups that also included specimens tested under quasi-static monotonic loading conditions [15,36]. The matrix, specifically designed to achieve chemical bond with the PBO fibers, was comprised of "high-fineness cement, an adhesion promoter, inorganic nanoparticles, microaggregates, and a polycar-boxylate water-reducing admixture" [39]. The matrix mechanical properties were determined by testing at least 2 cylinders from each batch used to cast the FRCM composite. The matrix average compressive strength and average tensile strength obtained were 28.4 MPa (CoV = 0.092) and 3.5 MPa (CoV = 0.231), respectively [15].

One LVDT was mounted to the concrete block on each side of the FRCM composite close to the loaded end. The LVDTs reacted off of a thin aluminum Ω-shaped plate bonded to the bare fibers immediately outside the bonded length (Fig. 1b). The average displacement measured by the two LVDTs is named *global slip g* in this paper and was used to control the quasi-static monotonic loading after the designated number of cycles as well as the quasi-static monotonic tests that were used as reference.

3. Quasi-static monotonic tests

The results of 26 single-lap quasi-static monotonic tests previously conducted by the authors using the same composite [36] are briefly summarized in this section (see Table 1). Quasi-static monotonic specimens with bonded length equal to 330 mm and different bonded widths, namely 43 mm (5 longitudinal fiber bun-dles), 60 mm (7 longitudinal fiber bundles), and 80 mm (9

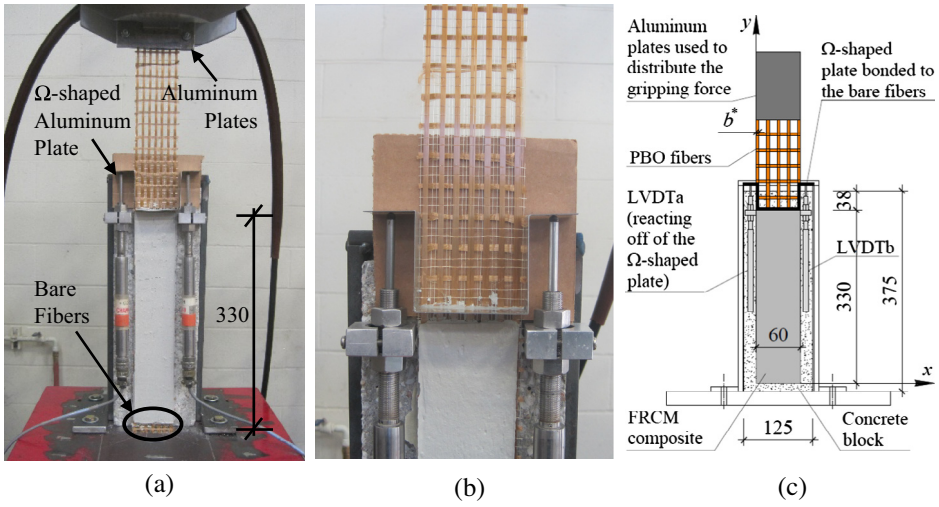

Fig. 1. (a) Photo of specimen DS_330_60_D_2. (b) Detail of the Ω-shaped aluminum plate in specimen DS_330_60_4. (c) Test set-up. (Dimensions in mm.)

Table 1
Results of the quasi-static monotonic tests.

Specimen	P^* [kN]	σ^* [MPa]	Specimen	P^* [kN]	σ^* [MPa]
DS_330_43_2^T	5.25	2280	DS_330_60_D_4	5.24	1630
DS_330_43_3	5.27	2290	DS_330_60_D_5	6.69	2080
DS_330_43_6	5.09	2210	DS_330_60_S_2	7.31	2270
DS_330_43_S_2^T	5.12	2230	DS_330_60_S_3	6.55	2030
DS_330_43_S_3^T	3.03	1320	DS_330_80_1	8.47	2050
DS_330_60_1^T	7.05	2190	DS_330_80_3	8.28	2000
DS_330_60_2^T	6.56	2040	DS_330_80_D_1	8.90	2150
DS_330_60_3^T	6.06	1880	DS_330_80_D_2	8.68	2100
DS_330_60_4^T	6.50	2020	DS_330_80_D_4	8.42	2030
DS_330_60_5^T	6.28	1950	DS_330_80_D_5	8.58	2070
DS_330_60_D_1	8.29	2580	DS_330_60_T_1	6.62	2060
DS_330_60_D_2	7.12	2210	DS_330_60_T_2	6.27	1950
DS_330_60_D_3	6.56	2040	DS_330_60_T_3	6.59	2050

Note on the nomenclature: DS_330_Y_(S, D, and/or T)_Z$^{(T)}$ where 330 indicates the bonded length in mm, Y = bonded width in mm, S = presence of strain gauges mounted on the fiber net, D = specimen tested until a constant load at the end of the test was measured, T = transversal bundles removed before applying the matrix, Z = specimen number, superscript T = transversal fiber bundles oriented toward the concrete block [36].

longitudinal fiber bundles) are considered in Table 1. Specimens with bonded width equal to 34 mm [15] were also tested but are not considered in this paper because their peak loads were particularly scattered, and the specimens presented a non-uniform distribution of the load among the different bundles [36]. In fact, the authors observed that non-uniform load distribution among the fiber bundles may occur as the impregnation of the fibers by the matrix is not easily controllable. As the non-uniform load distribution might lead to misinterpretation of the load response, only those specimens with a bonded width greater than 34 mm and tested under quasi-static monotonic conditions that reported a relatively even distribution of the applied load among the longitudinal fiber bundles [36] were considered as reference. Table 1 summarizes the results of the 26 tests selected. A note at the end of Table 1 explains the test specimen designation adopted in this paper.

The quasi-static monotonic tests were conducted in displacement control. The global slip g was used to control the tests and was increased at a constant rate equal to 0.00084 mm/s.

The failure of PBO FRCM-concrete joints under quasi-static monotonic load was characterized by debonding between the fiber and the embedding matrix [13–17,36]. The applied load P – global slip g curve for specimen DS_330_60_D_3, which is representative of the load response of the FRCM-concrete joints tested under quasi-static monotonic loading, is reported in Fig. 2a for reference, whereas an idealized applied load P – global slip g response, put forward by the authors, is reported in Fig. 2b [15,36]. It should be noted that the load response reported in Fig. 2b refers to a bonded length greater than the effective bond length, i.e. the min-imum length needed to fully establish the stress-transfer mecha-nism between the matrix and the fibers [15]. The load response is characterized by an initial linear branch followed by a non-linear branch up to the onset of debonding, which corresponds to the debonding load P_{deb} (Fig. 2). As the global slip g increases when $P > P_{deb}$, the stress-transfer mechanism is fully established, and the stress-transfer zone [40] translates along the bonded length toward the free end. The applied load P increases due to the presence of friction (interlocking) between single fiber fila-ments and between fibers and matrix [36] in the debonded region. When the residual bonded length is equal to the effective bond length the applied load attains the peak (ultimate) value P^*. After P^* the residual bonded length is shorter than the effective bond length, and the stress-transfer mechanism is no longer fully estab-lished. Hence, the applied load decreases with increasing g until it reaches the constant value P_f, which corresponds to the contribu-tion of friction alone.

The peak load values of the quasi-static monotonic tests were used to compute the peak stress σ^*:

$$\sigma^* = \frac{P^*}{nb^*t^*} \tag{1}$$

where n is the number of longitudinal bundles within the bonded width. The values of the peak load and corresponding peak stress are reported in Table 1 for each specimen considered. The average value of the peak stress $\bar{\sigma}^*$ obtained from the quasi-static mono-tonic tests is equal to 2070 MPa (CoV = 0.109).

The average peak load $\bar{P}^* = \bar{\sigma}^* n b^* t^*$, computed from the average peak stress $\bar{\sigma}^*$ = 2070 MPa, of the quasi-static monotonic tests (Table 1) with b_1 = 60 mm is equal to 6.65 kN.

Provided that the effective bond length and the contribution of friction between matrix and fibers and between fiber filaments are known, it is possible to compute the value of the debonding load P_{deb} [36]:

$$P_{deb} = P^* - \bar{\tau}_f \cdot 2 \cdot n \cdot b^* (\ell - \bar{l}_{eff}) \tag{2}$$

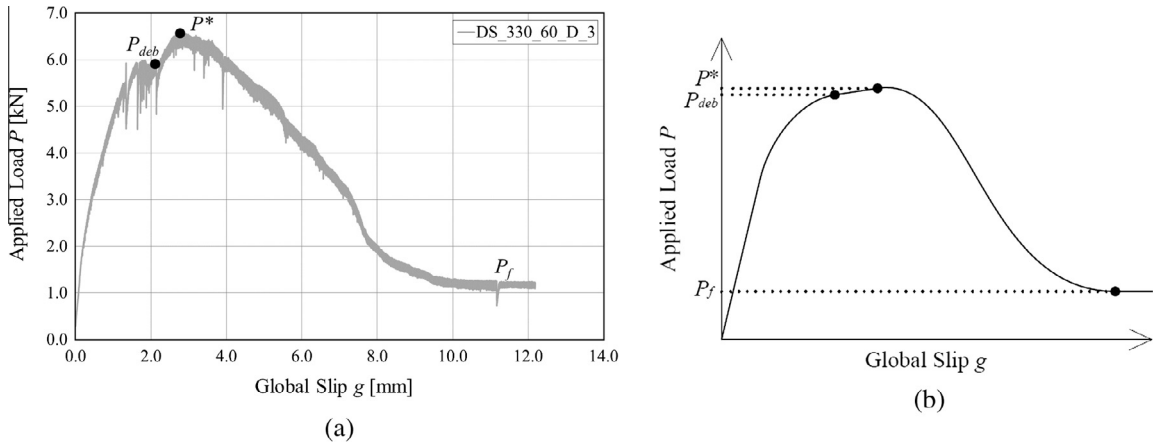

Fig. 2. (a) Applied load P – global slip g curve of specimen DS_330_60_D_3. (b) Idealized applied load P – global slip g response.

where ℓ and $\bar{l}_{eff}$ are the bonded length and the average effective bond length, respectively. $\bar{\tau}_f$ is the average shear stress associated with friction:

$$\bar{\tau}_f = \frac{\bar{P}_f}{2nb^*\ell} \tag{3}$$

where $\bar{P}_f$ is the average load value associated with friction. $\bar{P}_f$ was computed by averaging the values of the constant load measured at the end of the quasi-static tests of specimens marked with a D at the end of the specimen name (Table 1) and the resulting value of $\bar{\tau}_f$ was equal to 0.06 MPa. It should be noted that $\bar{\tau}_f$ was com-puted considering also specimens previously tested by the authors and not reported in Table 1 [36]. Strain profiles obtained from spec-imens equipped with strain gauges (Table 1) provided $\bar{l}_{eff} = 260$ mm [36]. Eq. (2) and the values of $\bar{\tau}_f$ and $\bar{l}_{eff}$ allowed for computing the value of the average debonding load $\bar{P}_{deb} = 6.36$ kN of specimens with $\ell = 330$ mm and with $b_1 = 60$ mm reported in Table 1.

4. Fatigue tests

Table 2 reports the results of 15 single-lap direct-shear fatigue tests conducted using different frequencies and load ranges. The fatigue loading protocol was designed to investigate the effects of different frequencies and different load ranges on: (a) the global slip g; (b) the dissipated energy during cycles; (c) the stiffness degradation of the interface; and (d) the post-fatigue quasi-static monotonic behavior. Specimens were initially subjected to a quasi-static monotonic load. In this initial loading stage (preload), the global slip was increased at a constant rate equal to 0.00084 mm/s. Once the *nominal* mean value $\bar{P}_n = (P_{n,\max} + P_{n,\min})/2$ of the prescribed load range was reached, a sinusoidal cyclic load was applied between nominal load levels $P_{n,\max}$ and $P_{n,\min}$, which define the nominal load amplitude $\Delta P_n = P_{n,\max} - P_{n,\min}$. Three nominal load ranges and three cycle frequencies were adopted. After the initial loading stage (preload), nine specimens (indicated in Table 2 with a P before the specimen number) were subjected to cyclic loading up to a prescribed number of cycles, after which the cyclic loading was stopped at a load value equal to $\bar{P}_n$. The specimens were subsequently tested under quasi-static monotonic loading condition. The global slip g was increased at a constant rate equal to 0.00084 mm/s up to a value of g of approx-imately 5 mm. Specimen DSF_1_20-65_P_1* was originally intended to be used to investigate the post-fatigue quasi-static monotonic response but failed prematurely before the prescribed number of cycles was completed. The remaining six specimens (out of 15), indicated in Table 2 with an F before the specimen number, were used to investigate the fatigue life of FRCM-concrete joints. Hence, after the initial loading stage (preload), those specimens were tested under cyclic condition up to failure with different frequencies and different nominal load ranges.

Five specimens each were tested under 1 Hz, 3 Hz, and 5 Hz sinusoidal loading. The frequency adopted is indicated in the spec-imen name as the number after the acronym DSF (Table 2). The

Table 2
Results of the fatigue tests.

Specimen	Total number of cycles (N or N_f)	$P_{\min}$ [kN] (CoV)	$P_{\max}$ [kN] (CoV)	$\bar{P}$ [kN] (CoV)	σ^* [MPa]	
DSF_1_20-50_P_1	23551	1.34 (0.001)	3.34 (0.001)	2.34 (0.000)	1810	×
DSF_1_20-50_P_2	26332	1.32 (0.002)	3.31 (0.006)	2.32 (0.001)	2140	√
DSF_1_20-65_P_1*	9152	1.34 (0.001)	4.33 (0.013)	2.84 (0.002)	–	–
DSF_1_20-65_P_2	25171	1.45 (0.002)	4.32 (0.008)	2.89 (0.001)	1940	√
DSF_1_35-65_P_1	38048	2.47 (0.001)	4.13 (0.001)	3.21 (0.001)	1720	√
DSF_3_20-50_P_1	124321	1.39 (0.002)	3.33 (0.010)	2.35 (0.004)	1600	√
DSF_3_20-50_P_2	117822	1.39 (0.014)	3.29 (0.026)	2.34 (0.002)	2110	×
DSF_3_20-65_F_1	55844	1.48 (0.020)	4.21 (0.074)	2.85 (0.005)	–	–
DSF_3_20-65_F_2	67544	1.47 (0.008)	4.30 (0.032)	2.89 (0.003)	–	–
DSF_3_35-65_P_1	120207	2.27 (0.002)	4.27 (0.002)	3.27 (0.001)	1540	×
DSF_5_20-50_P_1	204484	1.41 (0.006)	3.33 (0.009)	2.37 (0.006)	1350	√
DSF_5_20-50_F_1	803859	1.36 (0.017)	3.33 (0.039)	2.35 (0.007)	–	–
DSF_5_20-65_F_1	61547	1.53 (0.033)	4.16 (0.114)	2.84 (0.020)	–	–
DSF_5_35-65_F_1	134623	2.32 (0.005)	4.26 (0.011)	3.29 (0.004)	–	–
DSF_5_35-65_F_2	400444	2.31 (0.007)	4.24 (0.014)	3.28 (0.003)	–	–

Note on the nomenclature: DSF_X_M-H_F or P_Z$^{(*)}$ where X = frequency adopted in Hz, M = percentage of the peak load corresponding to $P_{n,\min}$, H = percentage of the peak load corresponding to $P_{n,\max}$, F = specimen subjected to fatigue loading until failure, P = specimen subjected to post-fatigue quasi-static loading, Z = specimen number, superscript * = specimen failed prematurely.

nominal load ranges considered in this study refer to the average peak load $\bar{P}^* = 6.65$ kN of the quasi-static tests with bonded length equal to 330 mm and bonded width equal to 60 mm as discussed above. The three nominal load ranges adopted were 20–50% (6 specimens), 20–65% (5 specimens), and 35–65% (4 specimens). Due to the sensitivity of the testing machine, the actual maximum and minimum applied loads varied during the cycles and therefore were slightly different from the nominal load values prescribed. The actual average maximum (P_{max}) and average minimum (P_{min}) applied load values of the fatigue cycles were computed averaging the maximum and minimum applied load values, respectively, obtained for selected ten-cycle blocks, as will be explained below. The values of P_{max}, P_{min}, and mean value $\bar{P}$ obtained are reported in Table 2 for each specimen together with their corresponding coefficient of variation (CoV).

The nominal load ranges 20–50%, 20–65%, and 35–65% computed in terms of $\bar{P}^*$ correspond to nominal load ranges 21–52%, 21–68%, and 37–68% in terms of the average debonding load $\bar{P}_{deb}$ = 6.36 kN, respectively.

5. Fatigue failure mode

All specimens subjected to cyclic loading until failure (specimens labeled with F in Table 2) failed due to the rupture of some fibers filaments within the bonded length. Since the load cycles were performed by controlling the force, when the specimens were no longer able to sustain the applied load range the fibers pulled out of the matrix in an attempt to reach the prescribed maximum applied load. As an example, the load response of specimen DSF_3_20-65_F_2 is reported in Fig. 3. It should be noted that at the end of the test the applied load P is almost constant and similar to the value corresponding to friction, P_f, observed in quasi-static tests of specimens with the same characteristics. This indicates the presence of friction (interlocking) between fibers and matrix and between fiber filaments, which in turn confirms that the matrix-fiber interface was damaged during the cyclic loading.

The application of the cyclic loading could have caused damage to the matrix-fiber interface. The fibers were probably cyclically damaged by friction between the fibers and matrix for the portion of the bonded length where debonding occurred. Rupture of embedded fiber filaments during the cyclic loading was difficult to observe, hence it is also possible that damage to the filaments occurred in the very last part of the test when the testing machine was trying to reach the prescribed applied load. However, failure of fiber filaments that were located within the bonded area was clearly visible at the end of the test (Fig. 4a). The presence of loose filaments within the bare fiber region (Fig. 4b), which was observed during the cycles, may indicate the rupture of fiber fila-ments within the bonded area during the cyclic loading.

It should be noted that the test set-up adopted might have influenced the fatigue response. In fact, as the fibers were left bare outside the bonded region, it is possible that during the descending branch of the fatigue cycles the slip gained could not be fully recovered, and the fibers were unloaded only in the portion outside the bonded area. In other words, the interfacial slip between the fibers and the two embedding layers of matrix gained during the ascending branch of the cycles could not be completely recovered when the load decreased because the bare fibers have negligible compression stiffness.

It is important to observe that after fatigue failure occurred almost all fiber filaments that extended beyond the bonded area at the free end (Fig. 1a) slipped inside the matrix (Fig. 4c), which suggests that the matrix-fiber interface was damaged along the entire bonded length.

Rupture of single fiber filaments outside the bonded area was observed for a limited number of specimens tested by the authors under quasi-static monotonic condition. Those failures, previously indicated as *stretching* of the bare fibers by the authors [17], were attributed to a non-uniform distribution of the applied force that resulted in a high stress level in one or more bundles that eventually led to the failure of the entire strip of fibers. Fig. 4d shows an exam-ple of the fiber stretching failure observed in the quasi-static mono-tonic tests. It should be pointed out that the fiber filament failure observed in the fatigue tests is a different phenomenon from that observed in the quasi-static tests. In the former, the fiber filaments failed within the bonded area due to increasing fatigue damage, whereas in the latter the fiber filaments failed outside the bonded area due to non-uniform load distribution among the different bun-dles. The different location of the fiber rupture can be inferred from the different position of the Ω-shaped bent plate at the end of the fatigue (Fig. 4a) and monotonic quasi-static tests (Fig. 4d).

In the case of FRCM-strengthened RC beams subjected to cyclic loading this phenomenon might be slightly different as the fibers are embedded within the matrix for the entire beam length. However, at those cross sections where through-thickness cracks in the matrix are present, a similar phenomenon to what was observed in the direct-shear tests herein presented could occur. A sketch of the debonding of the fibers from the embedding matrix after a through-thickness crack has formed is shown in Fig. 5. As a

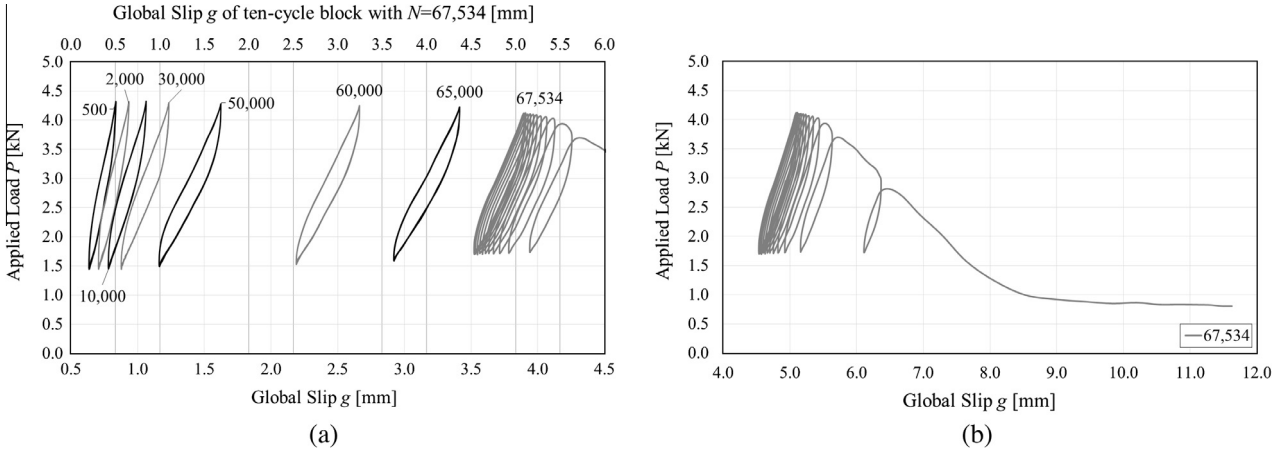

Fig. 3. (a) Selected ten-cycle blocks of specimen DSF_3_20-65_F_2 (the abscissas of the cycle block corresponding to N = 67,534 are placed on the top of the graph). (b) Failure of specimen DSF_3_20-65_F_2.

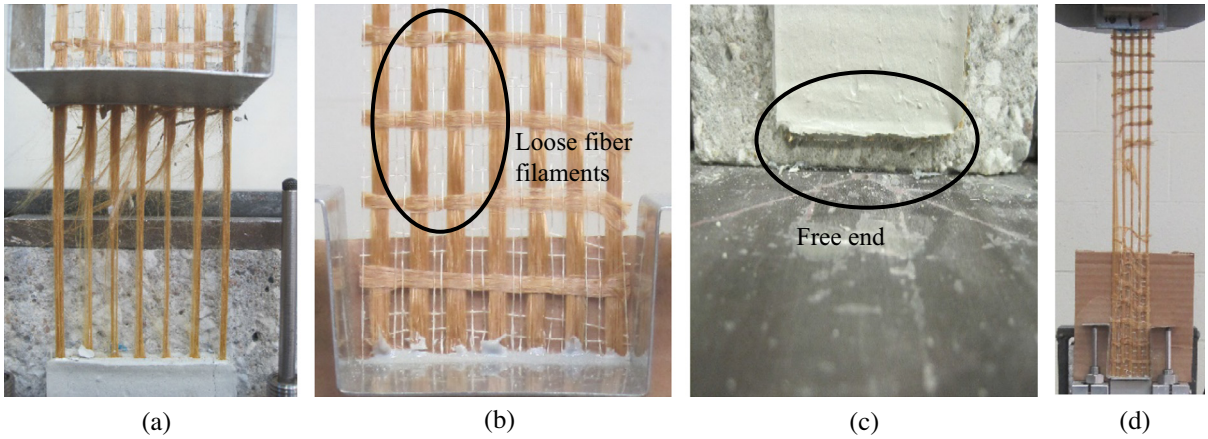

Fig. 4. (a) Fatigue failure of specimen DSF_5_35-65_F_1. (b) Detail of the bare fibers of specimen DSF_3_20-65_F_2. (c) Slippage of the fibers inside the matrix at the free end of specimen DSF_5_35-65_F_1. (d) Fiber stretching failure of specimen DS_330_43_4 [17].

flexural crack opens in the beam, a through-thickness crack forms in the matrix, and debonding at the matrix-fiber interface occurs because of compatibility. The presence of friction between the fibers and matrix and between fiber filaments may play an important role for long bonded lengths, as in case of full-scale beams. Fatigue tests on full-scale RC beams strengthened with FRCM composites and subject to cyclic loading are needed to confirm the results obtained from the single-lap direct-shear tests described in this paper.

The fatigue tests and the quasi-static monotonic tests were carried out in force and displacement control, respectively. In the quasi-static monotonic tests the evolution of the global slip and therefore the interfacial crack growth could be controlled. In the fatigue tests the applied force was controlled, thus when the specimen was no longer able to carry the prescribed load failure occurred suddenly. For this reason, differences in the failure modes of fatigue and quasi-static monotonic tests may also be due to the different test control employed. Further investigation is needed to analyze the stress-transfer mechanism during fatigue tests and to study the fatigue failure mode.

The premature failure of specimen DSF_1_20-65_P_1*, which was subjected to fatigue loading and intended to be used to investigate the post-fatigue quasi-static behavior, was characterized by debonding of the fibers from the matrix similarly to the failure observed in specimens tested until fatigue failure. DSF_1_20-65_P_1*, however, failed after a number of cycles substantially lower than other specimens with the same characteristics (see Table 2).

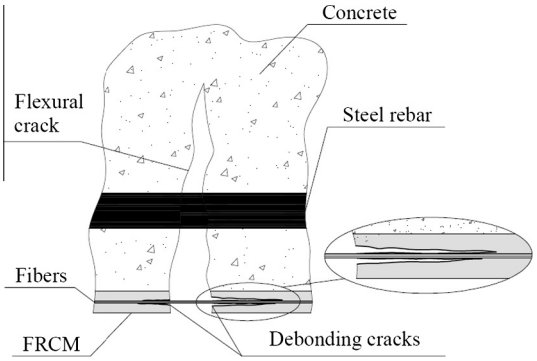

Fig. 5. Debonding at the matrix-fiber interface after a through-thickness crack in the matrix occurred.

6. Fatigue behavior

6.1. Global slip

The effect of the different frequencies and different load ranges adopted on the measured global slip g is investigated in Fig. 6. In this paper the global slip g is assumed to be related to the debonding crack a and crack growth, which were not directly measured. This assumption is confirmed by the behavior of specimens tested until failure, as explained below, and will be further discussed in this paper. The global slip plotted in Fig. 6 corresponds to the maximum applied load of each fatigue cycle. Specimen DSF_1_20-65_P_1*, which failed prematurely, is not reported in Fig. 6 and the remaining figures of the paper. Fig. 6a–c shows the g–N curves obtained for specimens with the same frequency (1 Hz, 3 Hz, and 5 Hz, respectively) and different load ranges. Comparing the behavior of specimens with different load ranges and frequency equal to 1 Hz (Fig. 6a), it can be observed that as the mean value $\overline{P}$ increases the global slip corresponding to P_{max} increases for a given number of cycles N. Values of $\overline{P}$ are reported in Table 2. This effect of the mean value P on the global slip for a given N is not confirmed by the g–N responses of specimens tested at 3 Hz (Fig. 6b) for which the global slip increased with ΔP rather than with P for a given N. The same trend is observed for specimens tested at 5 Hz (Fig. 6c). It should be noted that specimens tested at 1 Hz attained significantly different values of the global slip at the end of the preload phase, which might mislead the interpretation of the trend of Fig. 6a.

Fig. 6d–f shows the g–N curves obtained for specimens with the same nominal load ranges (20–50%, 20–65%, and 35–65%, respectively) and different frequencies. For nominal load range 20–50%g increased with frequency for a given number of cycles N. The behavior of specimens tested under 20–65% nominal load range resembles the behavior observed in case of specimens tested under 20–50% nominal load range.

The behavior observed for specimens tested with nominal load ranges 20–50% and 20–65% was also observed for specimens tested with nominal load range 35–65% (Fig. 6f). In the first part of the test the global slip g of specimen DSF_3_35-65_P_1 was higher than that of specimens with higher frequency. The global slip of specimen DSF_3_35-65_P_1 decreased for N = 1,000–5,000 (Fig. 6f), whereas it increased for N = 1–1,000 and N > 5,000. This can be attributed to the initial adjustment of the specimen that affected its behavior as discussed below.

In general, an initial adjustment of the specimens during the first cycles was observed. All fatigue tests featured a somewhat

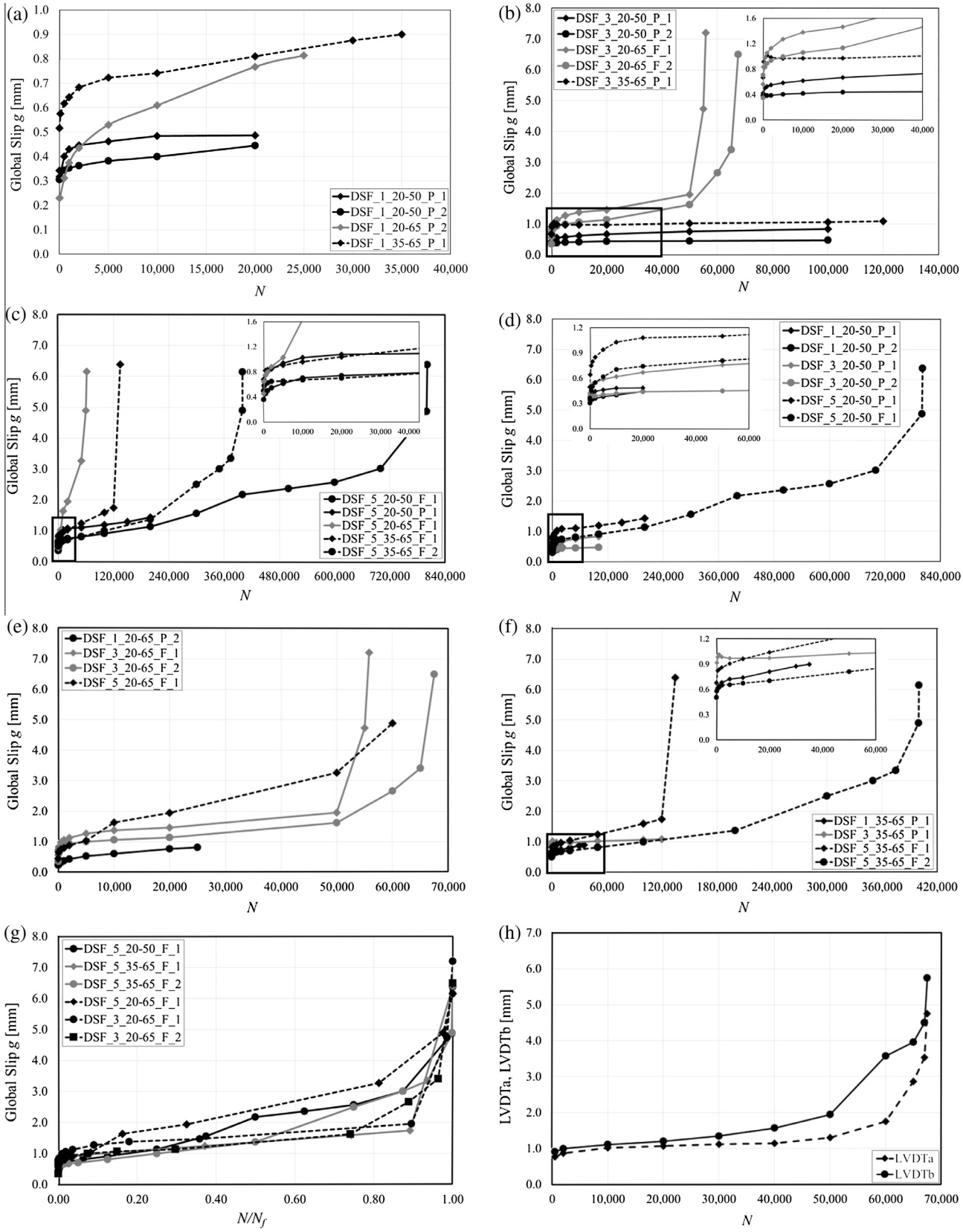

Fig. 6. Global slip–number of cycles N curves for fatigue specimens with frequency 1 Hz (a), 3 Hz (b), and 5 Hz (c). Global slip–number of cycles N curves for fatigue specimens with nominal load range 20–50% (d), 20–65% (e), and 35–65% (f). (g) Global slip–normalized number of cycles N/N_f for specimens tested until fatigue failure. (h) Displacement of the LVDTs vs. number of cycles N for specimen DSF_3_20-65_F_2.

irregular response from $N = 1$ up to $N = 500$. The following factors could explain this observation: (a) the stochastically distributed local variations of the matrix-fiber bond characteristics [38] may have led to a different behavior of the composite strip especially at the beginning of the test; and (b) high frequency in conjunction with high applied load level affected the initial adjustment of the specimens leading to a high level of damage of the matrix-fiber interface. The latter was confirmed by the results obtained from the specimens tested with high frequencies, which presented a glo-bal slip higher than that of specimens with lower frequencies even for the very first cycles ($N = 10–100$).

The global slip g is plotted versus the normalized number of cycles N/N_f in Fig. 6g. N_f is the number of cycles corresponding to fatigue failure. The plot of Fig. 6g includes all specimens that were intentionally tested to failure under cyclic loading. It can be observed that significant slip is gained during the very first cycles (approximately 2% of N_f). After that the rate of increase of the slip decreases considerably until approximately 90% of N_f when it sud-denly increases. This three-stage behavior resembles that observed in FRP-strengthened RC beams in terms of damage, steel strain, deflection, and crack propagation [31]. This observation suggests a relationship between the global slip and the length a of the inter-facial crack.

As noted in quasi-static monotonic tests previously conducted by the authors [36], the applied load is not always evenly dis-tributed among the longitudinal fiber bundles of the fiber net. Since the non-uniform distribution of the load among the different longitudinal bundles may lead to misleading results, the difference between the recorded displacements of LVDTa (left side of the bonded area) and LVDTb (right side of the bonded area, Fig. 1c) was computed for several ten-cycle blocks of each test. Fig. 6h shows the displacement measured by each LVDT during the fatigue cycles of specimen DSF_3_20-65_F_2. It can be observed that the difference between the displacements measured by the two LVDTs increased to approximately 1.5 mm (N = 60,000) and then decreased approaching the fatigue failure. This trend, which was observed in all specimens tested to fatigue failure, indicates that the non-uniform load distribution among the longitudinal bundles, caused by the stochastically distributed characteristic of the inter-face, may have contributed to the damage of the fibers caused by the fatigue cycles. According to the criteria previously adopted by the authors [36], only specimens DSF_3_20-65_F_2 and DSF_5_20-50_F_1 presented a relatively high non-uniform distri-bution (the former for the ten-cycle block corresponding to N = 60,000, the latter for the ten-cycle blocks corresponding to N = 700,000 and N = 800,000). Since the non-uniform load distribu-tion was limited to very few ten-cycle blocks close to N_f their results were considered reliable. All specimens designed to study the post-fatigue quasi-static behavior reported an even distribu-tion of the load among the longitudinal bundles during the fatigue loading, as per the criteria previously adopted by the authors [36]. However, for specimens DSF_1_20-50_P_1 and DSF_3_20-50_P_2 the readings of the two LVDTs were in opposite direction, which indicates a non-uniform load distribution.

6.2. Energy dissipation

A parameter of great interest for fatigue life assessment is the energy dissipated during the hysteresis cycles, which is repre-sented by the area included within the cycles in the $P–g$ diagram. For each specimen a block of ten fatigue cycles was considered for different values of N, and the area A_j within each ten-cycle block ($N = j$ and $N = j + 10$) was determined. As an example, the ten-cycle blocks of specimen DSF_3_20-65_F_2 are reported in Fig. 3a. The cycles up to $N = 500$ were disregarded due to the irregular behavior of the specimens as discussed earlier. For each specimen ten-cycle blocks were extracted at N = 500, 1,000, 2,000, 5,000, 10,000, 20,000, 50,000, and 100,000. Additional ten-cycle blocks were extracted every 100,000 cycles after N = 100,000 up to the maxi-mum number of cycles applied to each specimen. Additional ten-cycle blocks were selected to study the behavior of the speci-mens immediately before fatigue failure or interruption of the fati-gue loading. The cycles immediately before the fatigue failure, which were very irregular due to increasing damage (see Fig. 3b), were not considered. The same ten-cycle blocks extracted were also used to compute the average values of the applied load P_{max}, P_{min}, and the average mean value P (Table 2) and $\bar{\text{o}}$ determine the change in the slope of the fatigue cycles, which is presented in the next section. The area of each ten-cycle block considered was divided by the area corresponding to the ten-cycle block with $N = 500–510$, indicated as A_{500}, in order to study the change in the energy dissipation with respect to the beginning of the test. The area A_{500} was chosen because the initial cycles were irregular. The values of the normalized areas A_j/A_{500} are reported in Fig. 7 for different values of N. Fig. 7a–c allows for studying the effect of the different load ranges for a given frequency on the energy dis-sipated during each ten-cycle block. For specimens tested at 1 Hz, the increase in the energy dissipated with respect to the first 500 cycles was quite limited (Fig. 7a), except for specimen DSF_1_20-65_P_2, which presented an energy dissipation increase up to 70% with respect to the first 500 cycles. It should be noted that values of A_j lower than A_{500} are probably due to the values of P_{max} and P_{min}, which varied during the test with respect to $P_{n,max}$ and $P_{n,min}$, and to the method used to compute the ten-cycle block areas.

The results obtained for specimens tested at 3 Hz and 5 Hz (Fig. 7b and c, respectively) show the influence of the frequency on the initial behavior of the specimens. For specimens tested under 3 Hz the ratio A_j/A_{500} rapidly increased up to N = 20,000 and then increased with a reduced rate except for specimen DSF_3_20-50_P_2 for which the ratio A_j/A_{500} remained within 12% during the entire test. Specimens tested under 5 Hz reported a different behavior of the ratio A_j/A_{500} for the different applied load ranges. Specimen DSF_5_35-65_F_2, which failed at N = 400,404, shows an abrupt increase of the dissipated energy after 375,000 cycles. Specimens DSF_5_20-50_P_1 and DSF_5_20-50_F_1 presented a limited increase of the dissipated energy in the first 50,000 cycles, which is consistent with the results obtained with the same nominal applied load range and fre-quency equal to 1 Hz for the first 20,000 cycles (Fig. 7a and b). Finally, specimen DSF_5_20-65_F_1 showed a rapid increase in the ratio A_j/A_{500} in the first 10,000 cycles.

Comparing the specimens tested with the same nominal load ranges and different frequencies (Fig. 7d–f), it can be observed that in general the ratio A_j/A_{500} increased rapidly in the first part of the test, depending also on the frequency and the load range adopted, except for specimens DSF_3_20-50_P_2, as observed above, DSF_5_20-50_F_1, and DSF_5_35-65_F_2.

Although Fig. 7 does not present a clear effect of the load range and frequency on the ratio A_j/A_{500}, some of the plots suggest that an increase of the frequency or P_{max} implies an increase of the ratio A_j/A_{500} for a given number of cycles. It should be noted that the variation of P_{max} and P_{min} during the cycles might have influenced the value of the areas A_j.

6.3. Interfacial stiffness

The change in slope of the load response cycles can be related to the degradation of the stiffness of the matrix-fiber interface [37]. The ten-cycle blocks extracted to measure the energy dissipated during the cyclic loading were used to compute the slope k of

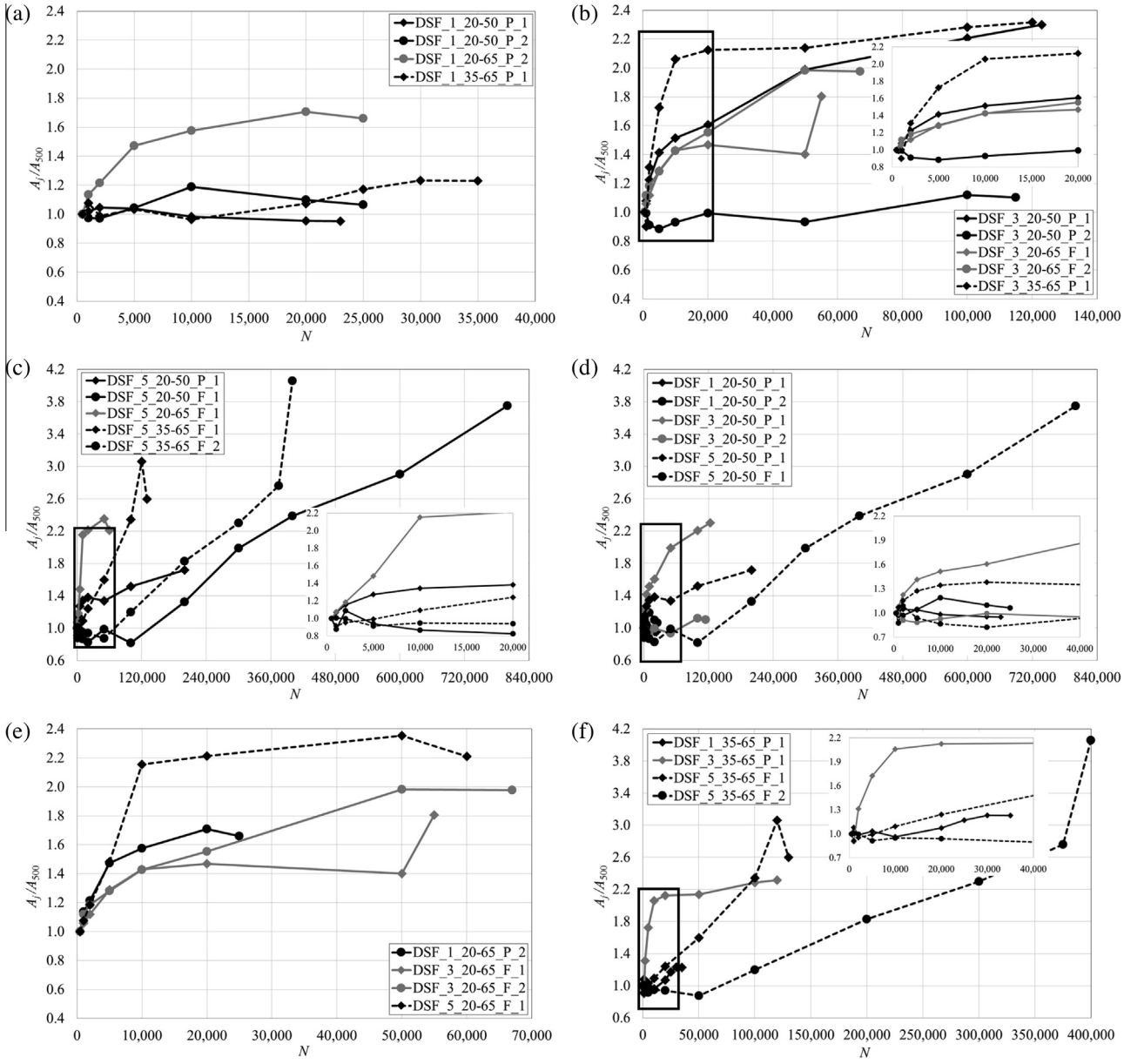

Fig. 7. A_j/A_{500}–N curves for fatigue specimens with frequency 1 Hz (a), 3 Hz (b), and 5 Hz (c). A_j/A_{500}–N curves for fatigue specimens with nominal load range 20–50% (d), 20–65% (e), and 35–65% (f).

the P–g response for different values of N. k was obtained as the slope of the line connecting the maximum and the minimum load of each ten-cycle block considered. Since the change of k during the fatigue cycles may be affected by the initial condition of the spec-imens and particularly by the initial stiffness of the matrix-fiber interface, the slope determined from the ten-cycle blocks was divided by the slope k_0, which is the slope of the first fatigue cycle ($N = 1$).

Fig. 8 reports the k/k_0–N curves obtained for fatigue specimens with the same frequency (Fig. 8a–c) and the same nominal load range (Fig. 8d–f). The ratio k/k_0 determined for specimens tested at 1, 3, and 5 Hz decreased rapidly in the first part of the test (first stage), whereas it leveled off afterwards (second stage). Fig. 8b and c shows that after the second stage, the ratio k/k_0 decreases again (third stage) although with a lower rate with respect to the first stage. The stiffness degradation appears to be more severe for specimens with larger load amplitude. Comparing the results of specimens with the same nominal load range and different frequencies (Fig. 8d–f) it can be observed that for specimens tested under lower load levels, namely those tested under a nominal applied load range of 20–50%, k/k_0 decreased rapidly up to values of N within 2000 and 5000, whereas it decreased at a lower rate afterwards (Fig. 8d). For specimens tested under a higher load range, namely those tested under nominal load range of 35–65% and 20–65%, k/k_0 decreased rapidly during the first 5000 cycles and kept decreasing at a lower rate with increas-ing N (Fig. 8e and f). A clear influence of the frequency adopted was not observed.

7. *S–N* curves and fracture mechanics fatigue model

The *cumulative fatigue damage* approach, which employs the S–N curves, also known as the Wöhler curves, is used to predict the fatigue life of structural elements. S–N curves can be constructed by plotting the amplitude of the applied stress range $\Delta\sigma$

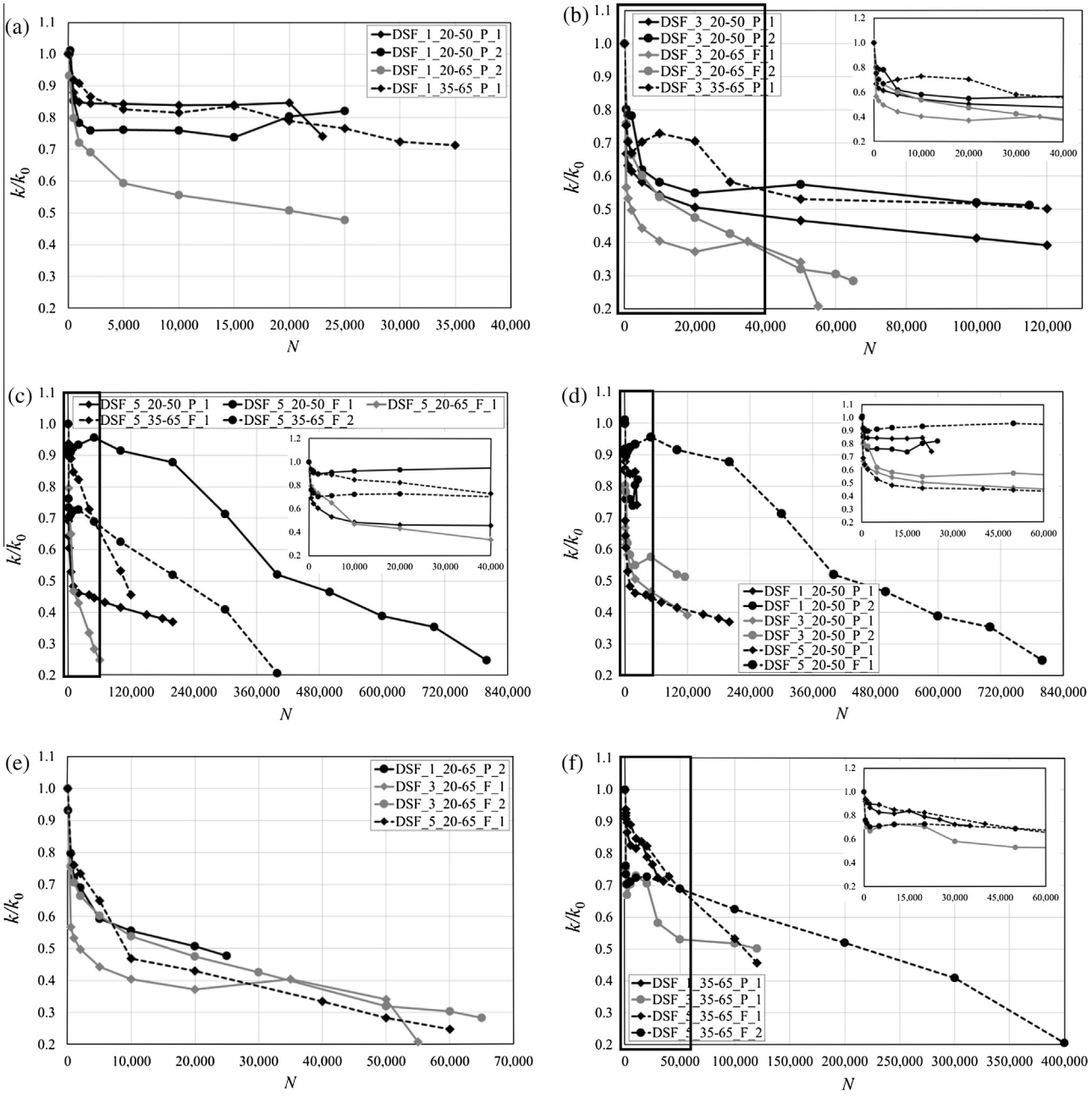

Fig. 8. k/k_0–N curves for fatigue specimens with frequency 1 Hz (a), 3 Hz (b), and 5 Hz (c). k/k_0–N curves for fatigue specimens with nominal load range 20–50% (d), 20–65% (e), and 35–65% (f).

[25] or the applied maximum stress σ_{max}, which is usually normalized with respect to the element strength [41], as a function of the number of cycles N to failure:

$$\Delta\sigma = (1 - R_W)\sigma_u N^{-\varphi} \quad (4)$$

$$\sigma_{max}/\sigma_u = 1 - \beta(1 - R_W)\log N \quad (5)$$

where $R_W = \sigma_{min}/\sigma_{max}$ is the loading ratio, σ_{min} is the applied minimum stress, σ_u is the strength of the material when subjected to quasi-static monotonic loading, and φ and β are coefficients that are determined from the experimental data. Eqs. (4) and (5) were used to fit the results obtained from the FRCM-concrete joints tested until fatigue failure (specimens with F before the specimen number in Table 2). σ_{max} and σ_{min} were computed through Eq. (1) considering P_{max} and P_{min}, respectively. σ_u was taken equal to $\sigma_{deb} = P_{deb}/(nb^*t^*)$. The values of φ determined for each R_W are very similar and equal to 0.037, 0.033, and 0.047 for R_W equal to 0.35, 0.41, and 0.54, respectively, whereas β was determined to be equal to 0.120. The values provided are specific for the tests and materials reported in this paper. Eqs. (4) and (5) are plotted in Fig. 9a and b, respectively, for the three values of R_W. It should be noted that the point $N = 1$ in Fig. 9b represents the quasi-static monotonic case. Although the results obtained with Eqs. (4) and (5) are promising, further tests are needed to confirm the validity of this approach. The limited number of tests does not allow for the investigation of, for example, whether a multilinear trend of the S–N curve is pos-sible or if a fatigue endurance limit exists.

The fatigue life can be also studied within the framework of fracture mechanics. In linear elastic fracture mechanics, the Paris law is a power law that relates the crack growth rate da/dN to the stress intensity factor range $\Delta K = K_{max} - K_{min}$ [42,43]. The

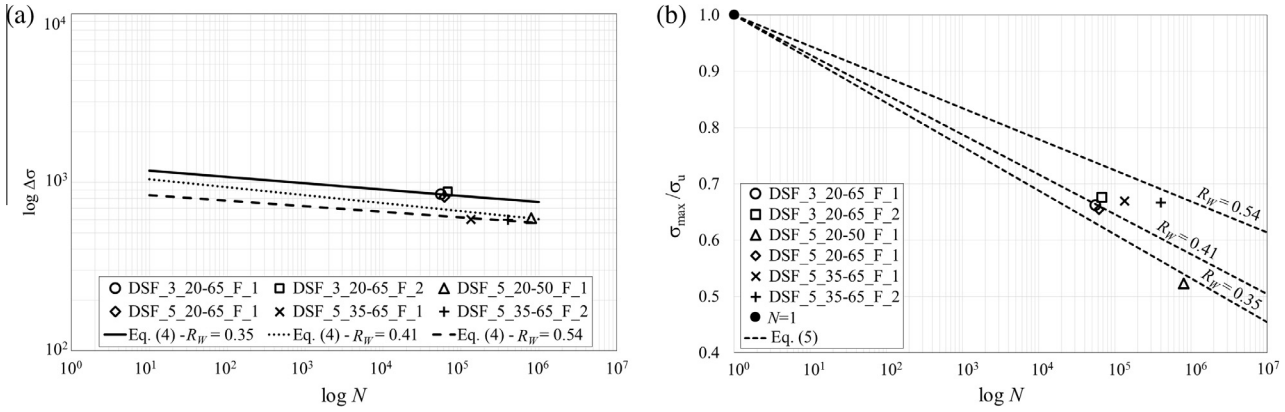

Fig. 9. (a) $\log\Delta\sigma - \log N$ Wöhler curve. (b) $\sigma_{max} - \sigma_u$ Wöhler curve.

Paris law provides a good approximation of the intermediate range of the fatigue crack growth, whereas it fails to describe the initial and final range of the fatigue crack growth. The Paris law has been employed by some authors in an attempt to describe the fatigue behavior of concrete and other brittle materials [43] and of concrete elements strengthened with FRP composites. Based on experimental observations of FRP-concrete joints Diab et al. [21] proposed a fracture mechanics model based on the Paris law that relates the interfacial crack growth rate, da/dN, to the energy ratio $G_F^{fatigue}/G_F$, where $G_F^{fatigue}$ is the energy release associated with the maximum load of the cycle, and G_F is the fracture energy associated with the debonding phenomenon under quasi-static monotonic loading. Carloni and Subramaniam [20] observed that the energy release rates employed by Diab et al. [21] are directly related to the corresponding applied load values and proposed a fracture mechanics model that takes into account the influence of the load amplitude and the applied load mean value. In this section, the approach employed by Carloni and Subramaniam [20] is extended by the authors to the case of FRCM-concrete joints. The crack propagation rate is related to the load amplitude and mean value in Eq. (6):

$$\frac{da}{dN} = m \cdot \xi \left(\frac{\sqrt{\Delta P \cdot \overline{P}}}{\mu \cdot (G_F^i + G_F^e)} \right)^{\omega \cdot \alpha} \gamma \tag{6}$$

The coefficients m and ω are determined from experimental results; ξ and α are coefficients related to the effect of the frequency on the crack growth; γ is a structural coefficient that takes into account the difference between the results obtained with direct-shear tests and real applications. Finally, μ is a coefficient that takes into account the presence of multiple matrix-fiber interfaces in the case of more than one layer of fibers (μ = 1.0 in the case of one fiber layer), assuming that the different fiber layers debond simultaneously. For the case of FRCM-concrete joints, two fracture energies G_F^i and G_F^e must be considered as it was recognized by the authors [36] that the fracture process involves two interfaces, namely the interface between the fibers and the internal layer of matrix and the interface between the fibers and the external layer of matrix. Results previously obtained by the authors showed that the internal matrix layer is responsible for most of the stress transfer. This is attributed to the different restraint conditions of the internal and external matrix layers: while the internal matrix layer is connected directly to the concrete, the external matrix layer is connected with the internal matrix layer only through the openings of the fiber net. The difference between the internal and external layer behavior was interpreted by the authors as a different cohesive law for the interfaces, which in turn entailed two different fracture energies [36].

As a first attempt to describe the intermediate range of the fatigue crack growth of FRCM-concrete joints, the global slip g can be associated to the debonding crack growth a, and Eq. (6) can be modified as:

$$\frac{dg}{dN} = m_1 \cdot \xi_1 \left(\frac{\sqrt{\Delta P \cdot \overline{P}}}{\mu_1 \cdot (G_F^i + G_F^e)} \right)^{\omega_1 \cdot \alpha_1} \gamma_1 \tag{7}$$

where the coefficients m_1, ξ_1, ω_1, α_1, γ_1, and μ_1 have the same meaning of m, ξ, ω, α, γ, and μ of Eq. (6), respectively. The assumption made in Eq. (7) requires further investigation as the global slip g includes a contribution associated with the elastic deformation of the debonded portion of the fibers.

The plots of the fatigue specimens (Fig. 6a–f) were used to compute the values of dg/dN. For each specimen dg/dN was computed in a discrete manner considering the ratio $\Delta g/\Delta N$ corresponding to pairs of subsequent ten-cycle blocks. Since Eq. (7) only describes the intermediate range of the fatigue crack growth, the ten-cycle blocks corresponding to the initial and final range were not considered. The intermediate ranges of the fatigue crack growth were defined for each load range with respect to the corresponding fatigue life observed in specimens tested until fatigue failure (Fig. 6g). The ten-cycle blocks considered during the analysis of the global slip behavior and included within 1.25–75%, 5–75%, and 8–83% of the fatigue life for specimens with load ranges 20–50%, 20–65%, and 35–65%, respectively, were considered to compute the values of $\Delta g/\Delta N$ corresponding to the intermediate crack growth range. For specimens that were interrupted or failed before the end of the intermediate crack growth stage, all ten-cycle blocks available from the onset of the intermediate crack growth stage were employed. A fatigue life corresponding to N_f = 800,000, N_f = 60,000, and N_f = 400,000 cycles was considered for specimens with load ranges 20–50%, 20–65%, and 35–65%, respectively. Specimens DSF_1_20-50_P_1 and DSF_3_20-50_P_2 were not con-sidered because the displacements measured by the two LVDTs were in opposite directions due to non-uniform load distribution. Furthermore, specimens DSF_3_35-65_P_1 and DSF_5_20-65_F_1 were disregarded because in the former the global slip decreased for certain values of N, which may have affected the slope dg/dN, whereas in the latter the intermediate range of the fatigue crack growth was not clearly recognizable. It should be noted that the values of N_f were determined from tests conducted at 3 and 5 Hz and the effect of the frequency on the fatigue life was neglected.

The average value of $\Delta g/\Delta N$ was used as representative of dg/dN for each specimen. γ_1 and μ_1 were taken equal to 1 because the results employed refer to single-lap direct-shear tests with one layer of fibers. The average values of G_F^i and G_F^e previously obtained by the authors from quasi-static tests [36] are 915 J/m^2 and

Table 3
Values of the coefficients obtained from the regression analysis of experimental results.

f [Hz]	$\log(m_1)$	ξ_1	ω_1	α_1
1	−6.89	0.60	4.91	1.03
3	−7.09	0.96	5.22	0.97
5	−7.11	1.00	5.06	1.00

143 J/m^2, respectively. For each frequency adopted the values of the coefficients m_1 and ω_1 were determined through a regression analysis of the fatigue test results setting ξ_1 and α_1 equal to 1.0 and are reported in Table 3. The values of the coefficients related to the frequency are computed in the next section.

8. Influence of load frequency on the fatigue behavior

If pure fatigue is considered, the fatigue crack growth is independent of the frequency. In practice, time-dependent crack growth occurs and affects the parameters of the Paris law [42]. Fig. 10a shows the relationship between dg/dN and the frequency adopted. For each specimen, as mentioned above, the ratio dg/dN was calculated as the average of the values of $\Delta g/\Delta N$. Fig. 10a indicates that dg/dN decreases with increasing frequency. Fig. 10b and c show the relationship between dg/dN and the fre-quency adopted maintaining the distinction between different load amplitudes and different load mean values, respectively. The influ-ence of the frequency for the load ranges adopted confirms what has been reported in the literature, even when the effect of ampli-tude and mean value of the load range are considered separately except for specimens with $P = 50\%$ for which it appears that the frequency did not affect dg/dN.

Assuming that ξ_1 and α_1 are equal to 1.0 when the frequency is equal to 5 Hz, as it was previously assumed by other authors in case of FRP-concrete joints [21], it is possible to determine the values of ξ_1 and α_1 for each frequency adopted. The values of ξ_1 and α_1 obtained for frequencies equal to 1 Hz and 3 Hz are reported in Table 3. Fig. 10d shows the logarithmic relationship between dg/dN and $\sqrt{\Delta P \cdot \overline{P}}/(G_F^i + G_F^e)$ for each frequency adopted using the parameters of Table 3 and setting ξ_1 and α_1 equal to 1.0. It can be noted that the value of dg/dN decreases with frequency, as reported in the literature [26–28], for a given value of $\sqrt{\Delta P \cdot \overline{P}}/(G_F^i + G_F^e)$. Eq. (7) can be used to describe the behavior of dg/dN for any frequency f if the relationships $\alpha_1 = \alpha_1(f)$ and $\xi_1 = \xi_1(f)$ are established from the values of Table 3 and the values of ω_1 and m_1 corresponding to $f = 5$ Hz are employed. It should be noted that the values of α_1 are very similar to one another, whereas the estimated values of ξ_1 appear to increase with the frequency, suggesting that the frequency primarily affects the value of dg/dN rather than its rate with respect to the ratio $\sqrt{\Delta P \cdot \overline{P}}/(G_F^i + G_F^e)$.

9. Post-fatigue quasi-static tests

Eight of the 15 specimens presented in this paper were subjected to cyclic loading up to a prescribed number of cycles and then were tested under quasi-static monotonic loading condition to study the influence of the cyclic loading on the load response. The number of cycles applied before the quasi-static test was related to the frequency adopted and was approximately $N = 25{,}000$, $N = 125{,}000$, and $N = 200{,}000$ for the 1 Hz, 3 Hz, and 5 Hz specimens, respectively. The load response of specimen DSF_3_20-50_P_1, which is representative of the post-fatigue load

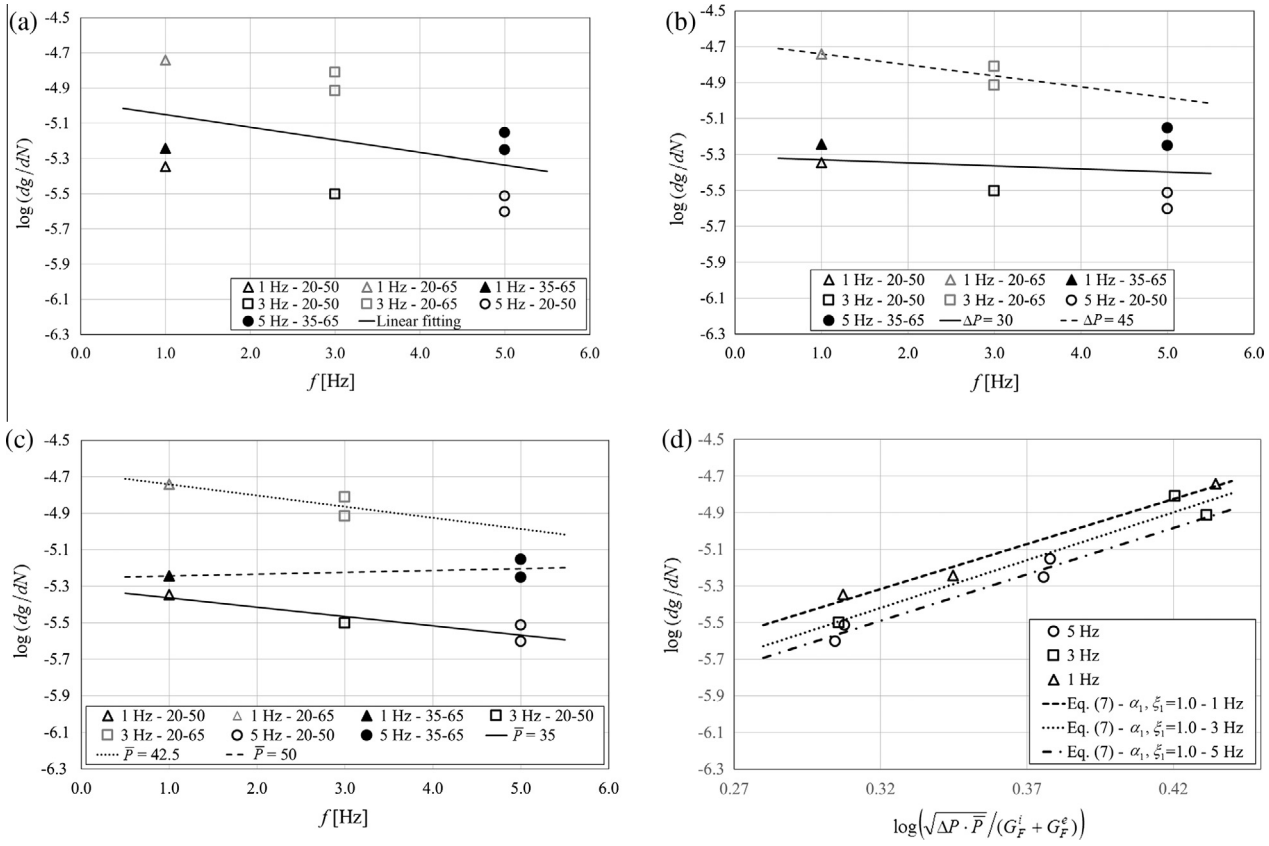

Fig. 10. Relationship between dg/dN and frequency adopted for all load ranges (a), for different load amplitudes (b), and different mean load values (c). (d) Relationship between dg/dN and $\sqrt{\Delta P \cdot \overline{P}}/(G_F^i + G_F^e)$.

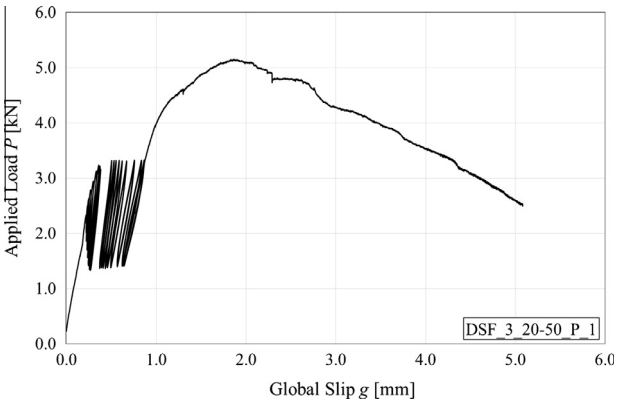

Fig. 11. Load response of specimen DSF_3_20-50_P_1.

responses obtained, is reported in Fig. 11. Fig. 11 also reports the preload phase and the ten-cycle blocks used to study the fatigue behavior. The peak load P^* was used to compute the peak stress σ^* (Eq. (1)), which is reported in Table 2 for each specimen tested under monotonic quasi-static condition after the cyclic loading was terminated. The shape of the post-fatigue load response resembles the shape of the load response of the quasi-static monotonic load response shown in Fig. 2a.

Since a non-uniform load distribution along the bonded width was reported for FRCM composites tested under quasi-static load [17,36], only the specimens that during the post-fatigue quasi-static loading reported a relatively even load distribution among the fiber bundles [36] were considered reliable for the com-parison. The load distribution among the bundles was investigated by computing the difference between the displacements recorded by the two LVDTs as mentioned above [36]. Specimens that reported an even load distribution are indicated in the last column of Table 2 with $\surd$ whereas specimens disregarded are indicated with $\times$. Fig. 12 reports the peak stress of each reliable specimen with respect to the number of cycles applied, which is reported next to each marker. The average value of the peak stress $\bar{\sigma}^* = 2070$ MPa for the quasi-static monotonic tests presented in Table 1 and the corresponding standard deviation $\bar{\sigma}^{*\pm}$ = 225 MPa are marked in Fig. 12 to investigate the effect of the fatigue cycles on the post-fatigue peak load. It was observed that the post-fatigue behavior of FRP-concrete joints is not influenced by a cyclic loading if the residual bonded length is longer than the effective bond length [37]. For FRCM-concrete joints, on the other hand, the peak stress is due not only to the bond between the matrix and fibers but also to the friction between the matrix and fibers and between fiber filaments [15]. However, the contribution of friction, which

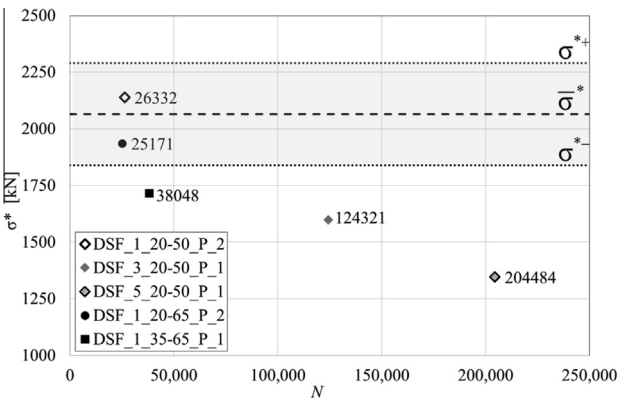

Fig. 12. Peak stress σ^* of post-fatigue quasi-static tests vs. number of fatigue cycles N applied.

can be computed if $\bar{\tau}_f$ and $\bar{l}_{eff}$ are known [36], is limited when com-pared to $\bar{\sigma}^*$ for the specimens considered. In fact, the contribution of friction to the peak load P^* for specimens with bonded length equal to 330 mm is approximately 90 MPa and is lower than the value of the standard deviation $\bar{\sigma}^{*\pm}$ = 225 MPa. Assuming that the contribution of friction is not affected by the fatigue loading, the peak stress obtained from post-fatigue quasi-static tests can be used instead of the debonding stress σ_{deb} to investigate the effect of the fatigue cycles on the load-carrying capacity of the FRCM-concrete joints tested.

Three specimens reported a value of the peak stress not included within the standard deviation of $\bar{\sigma}^*$ ($\bar{\sigma}^{*\pm}$ = 225 MPa), which suggests that the bonded length not damaged by the cyclic loading was shorter than the effective bond length. These specimens show a decrease of the post-fatigue peak stress with an increasing num-ber of cycles (Fig. 12). Two specimens, namely DSF_1_20-50_P_2 and DSF_1_20-65_P_2, reported a value of the peak stress included

within the standard deviation of $\bar{\sigma}^*$ ($\bar{\sigma}^{*\pm}$ = 225 MPa), which might indicate that the residual bonded length after the cycles was longer than the effective bond length. Both these specimens were tested at 1 Hz, and the fatigue tests were stopped after approximately 25,500 cycles. Comparing the results of specimens with frequency equal to 1 Hz that were subjected to a similar number of cycles before the quasi-static test, namely DSF_1_20-50_P_2, DSF_1_20-65_P_2, and DSF_1_35-65_P_1, it appears that the larger mean value P is associated with the greater damage of the interfacial bond.

Additional tests are needed to further investigate the effect of cycling loading with different amplitudes and mean values on the post-fatigue load response.

10. Conclusions

This paper presents and discusses the results obtained from an experimental campaign conducted on PBO FRCM-concrete joints tested under cyclic and post-fatigue quasi-static loading. The effect of different frequencies and load ranges was investigated with respect to the fatigue and post-fatigue behavior. Based on the results obtained, the following conclusions can be drawn:

- Fatigue failure of PBO FRCM-concrete joints is caused by rupture of the fibers within the bonded area. This type of failure was different from the rupture of fibers observed in a limited number of specimens previously tested under quasi-static monotonic loading by the authors. In fact, the former appears to be caused by the cyclic loading while sub-critical crack propagation occurs, whereas the latter is mainly caused by the non-uniform load distribution among the longitudinal bundles.
- In general, it was observed that the combination of high amplitude and high mean value of the load range implies greater damage measured in terms of global slip, energy dissipation, and interfacial stiffness degradation. The load frequency also appears to affect the fatigue response. In general, a decrease of the damage rate with increasing frequency measured in terms of dg/dN was observed.
- The use of a fracture mechanics approach that takes into account the influence of the frequency on the rate dg/dN allowed for describing the intermediate range of the fatigue crack growth in PBO FRCM-concrete joints. The results obtained confirmed that the frequency affects the fatigue life as reported in the literature.
- The effect of cycles on the quasi-static post-fatigue behavior of the PBO FRCM-concrete joints was investigated. The results suggest that an increase of the mean applied load value entails an increase of the interfacial damage. Further, the interface is rapidly damaged even for a relatively small number of cycles.

- Since tests conducted on FRCM composites may present a large variability due to the stochastically distributed property of the matrix-fiber interface, further tests are needed to confirm the observations reported in this paper.

Acknowledgements

The experimental work discussed in this paper was conducted at Missouri University of Science and Technology (Missouri S&T). The authors would like to express their appreciation to the National University Transportation Center (NUTC) at Missouri S&T for providing financial support for this project. Ruredil S.p.A. of San Donato Milanese, Italy, is gratefully acknowledged for providing the composite materials.

References

[1] D'Ambrisi A, Focacci F. Flexural strengthening of RC beams with cement based composites. J Compos Constr, ASCE 2011;15(2):707–20.
[2] Pellegrino C, D'Antino T. Experimental behaviour of existing precast prestressed reinforced concrete elements strengthened with cementitious composites. Compos Part B: Eng 2013;55:31–40.
[3] Pellegrino C, D'Antino, T. Failure due to delamination in concrete elements strengthened with cementitious composites. In: Proceedings of the 8th international conference on fracture mechanics of concrete and concrete structures (FraMCoS-8), Toledo, Spain, 10–14 March, 2013. p. 138–43.
[4] Ombres L. Debonding analysis of reinforced concrete beams strengthened with fibre reinforced cementitious mortar. Eng Fract Mech 2012;81:94–109.
[5] Toutanji H, Deng Y. Comparison between organic and inorganic matrices for RC beams strengthened with carbon fiber sheets. J Compos Constr, ASCE 2007;11(5):507–13.
[6] Orosz K, Täljsten B, Fischer G. CFRP strengthening with mineral based composites loaded in shear. In: Proceedings of the 8th international symposium on fiber reinforced polymer reinforcement for concrete structures, FRPRCS-8, Patras, Greece, 16–18 July, 2007.
[7] Blanksvärd T, Täljsten B, Carolin A. Shear strengthening of concrete structures with the use of mineral-based composites. J Compos Constr, ASCE 2009;13(1):25–34.
[8] Ombres L. Structural performance of reinforced concrete beams strengthened in shear with a cement based fiber composite material. Compos Struct 2015;122:316–29.
[9] Triantafillou TC, Papanicolaou CG, Zissinopoulos P, Laourdekis T. Concrete confinement with textile-reinforced mortar jackets. ACI Struct J 2006;103(1):28–37.
[10] Ombres L. Confinement effectiveness in concrete strengthened with fiber reinforced cement based composite jackets. In: Proceedings of the 8th international symposium on fiber reinforced polymer reinforcement for concrete structures, FRPRCS-8, Patras, Greece, 16–18 July, 2007.
[11] Peled A. Confinement of damaged and nondamaged structural concrete with FRP and TRC sleeves. J Compos Constr, ASCE 2007;11(5):514–22.
[12] Bournas DA, Triantafillou TC, Zygouris K, Stavropoulos F. Textile-reinforced mortar versus FRP jacketing in seismic retrofitting of RC columns with continuous or lap-spliced deformed bars. J Compos Constr, ASCE 2009;13(5):360–71.
[13] D'Ambrisi A, Feo L, Focacci F. Bond-slip relations for PBO-FRCM materials externally bonded to concrete. Compos Part B: Eng 2012;43(8):2938–49.
[14] D'Ambrisi A, Feo L, Focacci F. Experimental analysis on bond between PBO-FRCM strengthening materials and concrete. Compos Part B: Eng 2013;44(1):524–32.
[15] D'Antino T, Carloni C, Sneed LH, Pellegrino C. Matrix-fiber bond behavior in PBO FRCM composites: a fracture mechanics approach. Eng Fract Mech 2014;117:94–111.
[16] D'Antino T, Sneed LH, Carloni C., Pellegrino C. Bond behavior of the FRCM-Concrete Interface. In: Joaquim Barros, José Sena-Cruz, editors. Proceedings of the XI int. symp. on fiber reinforced polymers for reinforced concrete structures (FRPRCS11), , Guimarães, Portugal,; 2013.
[17] Sneed LH, D'Antino T, Carloni C. Investigation of bond behavior of PBO fiber-reinforced cementitious matrix composite-concrete interface. ACI Mater J 2014;111(5):569–80.
[18] D'Antino T, Pellegrino C, Carloni C, Sneed LH. Experimental analysis of the bond behavior of glass, carbon, and steel FRCM composites. Key Eng Mater 2015;624:371–8.
[19] Kim YJ, Heffernan PJ. Fatigue behavior of externally strengthened concrete beams with fiber-reinforced polymer: state of the art. J Compos Constr 2008;12(3):246–56.
[20] Carloni C, Subramaniam KV. Investigation of sub-critical fatigue crack growth in FRP/concrete cohesive interface using digital image analysis. Compos Part B: Eng 2013;51:35–43.
[21] Diab HM, Wu Z, Iwashita K. Theoretical solution for fatigue debonding growth and fatigue life prediction of FRP-concrete interfaces. Adv Struct Eng 2009;12(6):781–92.
[22] American Concrete Institute (ACI). Guide for the design and construction of externally bonded FRP systems for strengthening of concrete structure. ACI 440.2R-08. Mich. Farmington Hill; 2008.
[23] Japan Society of Civil Engineers (JSCE). Recommendations for upgrading of concrete structures with use of continuous fiber sheets. Concrete engineering, vol. 41, Tokyo; 2001.
[24] Harries KA, Aidoo J. Debonding- and fatigue-related strain limits for externally bonded FRP. J Compos Const, ASCE 2006;10(1):87–90.
[25] Plekhov O, Paggi M, Naimark O, Carpinteri A. A dimensional analysis interpretation to grain size and loading frequency dependencies on Paris and Wöhler curves. Int J Fatigue 2011;33:477–83.
[26] Zhang B, Phillips DV, Wu K. Effects of loading frequency and stress reversal on fatigue life of plain concrete. Mag Concr Res 1996;48:361–75.
[27] Saucedo L, Yu LC, Medeiros A, Zhang X, Ruiz G. A probabilistic fatigue model based on the initial distribution to consider frequency effect in plain and fiber reinforced concrete. Int J Fatigue 2013;48:308–18.
[28] Medeiros A, Zhang X, Ruiz G, Rena CY, Velasco MDSL. Effect of the loading frequency on the compressive fatigue behavior of plain and fiber reinforced concrete. Int J Fatigue 2015;70:342–50.
[29] Naik TR, Singh SS. Fatigue property of concrete with and without mineral admixtures. ACI 1994;SP 144-14:269–88.
[30] Gheorghiu C, Labossiere P, Proulx J. Response of CFRP-strengthened beams under fatigue with different load amplitudes. Constr Build Mater 2007;21:756–63.
[31] Kim YJ, Heffernan J. Fatigue behavior of externally strengthened concrete beams with fiber-reinforced polymers: state of the art. J Compos Constr, ASCE 2008;12(3):246–56.
[32] Oh BH. Fatigue-life distributions of concrete for various stress levels. ACI Mater J 1991;88(2):122–8.
[33] Aidoo J, Harries KA, Petrou MF. Fatigue behavior of carbon fiber reinforced polymer-strengthened reinforced concrete bridge girders. J Compos Constr, ASCE 2004;8(6):501–9.
[34] Sena-Cruz JM, Barros JAO, Coelho MRF, Silva RFFT. Efficiency of different techniques in flexural strengthening of RC beams under monotonic and fatigue loading. Constr Build Mater 2012;29:175–82.
[35] Ferrier E, Bigaud D, Hamelin P, Bizindavyi L, Neale KW. Fatigue of CFRPs externally bonded to concrete. Mater Struct 2005;38:39–46.
[36] Carloni C, D'Antino T, Sneed LH, Pellegrino C. Role of the matrix layers in the stress-transfer mechanism of FRCM composites bonded to a concrete substrate. J Eng Mech, ASCE 2014. http://dx.doi.org/10.1061/(ASCE)EM.1943-7889.0000883.
[37] Carloni C, Subramaniam KV, Savoia M, Mazzotti C. Experimental determination of FRP-concrete cohesive interface properties under fatigue loading. Compos Struct 2012;94:1288–96.
[38] Sneed LH, D'Antino T, Carloni C, Pellegrino C. A comparison of the bond behavior of PBO-FRCM composites determined by double-lap and single-lap shear tests. Cem Concr Compos. http://dx.doi.org/10.1016/j.cemconcomp.2015.07.007 [accepted for publication].
[39] Nanni A. A new tool for concrete and masonry repair – strengthening with fiber-reinforced cementitious matrix composites. Concr Int 2012;34:43–9.
[40] Carloni C, Subramaniam KV. Application of fracture mechanics to debonding of FRP from RC members. ACI 2012;SP-286. 10-1-10-14.
[41] Tepfers R, Kutti T. Fatigue strength of plain, ordinary, and lightweight concrete. ACI J 1979(May):635–52.
[42] Paris P, Erdogan F. A critical analysis of crack propagation laws. J Basic Eng, Trans Am Soc Mech Eng 1963(December):528–34.
[43] Bazant ZP, Planas J. Fracture and size effect in concrete and other quasi-brittle materials. Boca Raton, Florida: Springer; 1997.